Int. J. Therm. Sci. (1999) 38, 879–891

Thermal, physico-chemical and rheological boundary layers in multi-component oxidic melt spreads

Christophe Journeau*, François Sudreau, Jean-Marie Gatt, Gérard Cognet

Direction des réacteurs nucléaires, Commissariat à l'énergie atomique, CEA Cadarache, 13108 Saint-Paul-lez-Durance cedex, France

(Received 12 January 1999, accepted 13 April 1999)

Abstract — In the unlikely case of a severe accident in a nuclear reactor, the core material could melt and form a molten mixture named *corium*. The CEA has undertaken a large program to improve knowledge on corium behaviour. An experiment in which 17 kg of simulant corium — mainly made of hafnon, zircon, silica and wüstite — at more than 2 200 K, was spread in the VULCANO facility, is described. It is analysed in terms of thermal cooling by fitting the pyrometric measurements with outputs of a conduction code. This enables the estimation of temperature profiles inside the corium. From physicochemical modelling, the solid fraction, density and viscosity can be estimated. Thermal, physicochemical and rheological boundary layers are thus found. The rheological boundary layer is very steep (exponential decay parameter around 800 m^{-1}) and could significantly affect the flow dynamics. A visible aspect of this boundary layer is the presence of folds on the corium surface, similar to those on ropy pahoehoe lavas. © 1999 Éditions scientifiques et médicales Elsevier SAS.

conduction / boundary layers / viscosity / rheology / solidification / molten oxides / experiments / modelling / thermophysical properties

Résumé — **Couches limites thermiques, physico-chimiques et rhéologiques lors de coulées de bains de mélanges d'oxydes.** Dans le cas hypothétique d'un accident grave de réacteur nucléaire, les matériaux fondus du cœur formeraient un magma dénommé *corium*. Le CEA a entrepris un grand programme expérimental pour améliorer la connaissance du comportement du corium. On a réalisé une expérience au cours de laquelle 17 kg d'un corium simulant — composé principalement de hafnie, zircone, silice et wüstite — à plus de 2 200 K ont été étalés. Elle a été analysée sur le plan thermique en recalant les mesures pyrométriques avec les sorties d'un code de conduction. Ceci nous a permis d'estimer les profils de température dans le corium. À l'aide d'une modélisation physico-chimique, on peut en déduire la fraction de solide, la densité et la viscosité du mélange. Des couches limites thermiques, physico-chimiques et rhéologiques sont observées dans les premiers millimètres sous la surface. La couche limite rhéologique est marquée par des variations très rapides de la viscosité correspondant à un taux de décroissance exponentielle de l'ordre de 800 m^{-1}, ce qui peut avoir un effet sensible sur la dynamique de l'écoulement. Une conséquence visible de cette couche limite est la présence de plis à la surface du corium, semblables à ceux de certaines laves de type pahoehoe. © 1999 Éditions scientifiques et médicales Elsevier SAS.

conduction / couches limites / viscosité / rhéologie / solidification / bains d'oxydes / expérimentation / modélisation/ propriétés thermophysiques

Nomenclature

Roman letters

a	rheological parameter	K^{-1}
c	specific heat	$J \cdot kg^{-1} \cdot K^{-1}$
H	enthalpy	$J \cdot kg^{-1}$
H	height	m
i	mesh index	
$\mathcal{L}$	folds length	m
L	latent heat of fusion	$J \cdot kg^{-1}$
T	temperature	K
t	time	s

Greek letters

γ	exponential decay parameter	m^{-1}
δx	mesh dimension	m

* Correspondence and reprints.
cjourneau@cea.fr

δt	time increment	s
κ	thermal diffusivity	$m^2 \cdot s^{-1}$
λ	thermal conductivity	$W \cdot m^{-1} \cdot K^{-1}$
μ	dynamic viscosity	Pa·s
ξ_s	solid volume fraction in interface mesh	
ρ	specific mass	$kg \cdot m^{-3}$
ϕ	solid volume fraction	
Ψ	ratio of solidification and advection characteristic times	

1. INTRODUCTION

Within the framework of Pressurised Water Nuclear Reactor (PWR) severe accident studies, scenarios leading to partial or whole core melting, even if they are highly unlikely, cannot be excluded. In this case, a molten mixture called *corium*, essentially composed of highly refractory materials (UO_2, ZrO_2) and metals (Fe, Zr) may flow down towards the lower head of the reactor pressure vessel and, if there is no intervention, melt through the vessel and spread into the reactor pit.

For the new European Pressurized water Reactor (EPR), a collaboration between the French and German industries, great emphasis has been put on the development of specific features for severe accident prevention and mitigation [1]. In particular, a dedicated area of about 175 m^2 will be devoted to corium spreading. The bottom and lateral structures of this compartment have protection layers designed for the thermal loads.

In France, the Nuclear Reactor Division of the Atomic Energy Commission (CEA/DRN) has undertaken a large program [2] to improve the knowledge on corium, more specifically on long-term corium retention and coolability. This program is based on experimental and theoretical investigations, the results of which are ultimately to be used in scenario and mechanistic computer codes.

This paper is based on the physicochemical and thermal analysis of a simulant corium spreading test (VE-07). During the spreading of corium onto a substratum, there is a fast cooling of the corium lower and upper interfaces, while the inner flow remains hotter and thus less viscous than the boundary layers. The comparison of numerical simulations using the CRUST [3] thermal conduction code and experimental surface temperature measurements gives an insight into the thermal behaviour of an oxidic melt spread. This can then be combined with information on the physicochemical and thermophysical properties of the oxidic mixture. Special attention has been given to the analysis of viscosity. Boundary layers are defined in terms of thermal, physico-chemical and rheological properties. The rheological boundary layer is shown to be related to the presence of folds on the surface of the spread.

This work is restricted to a monodimensional approach of the cooling and solidification of the melt assumed to be at rest. The dynamics of the VULCANO spreading experiments have been presented in another paper [4] and compared to the simplified spreading model proposed by Griffiths and Fink [5].

2. DESCRIPTION OF THE EXPERIMENT

2.1. Test facility

The VULCANO facility (*figure 1*) is mainly composed of a furnace and a test section, the geometry and nature of which depend on the specific objectives of each experiment. The furnace, which is based on a plasma arc technique [6], has been designed to heat up to 3 000 K, and consequently to melt roughly one hundred kilograms of corium composed of representative or simulant materials: UO_2, HfO_2, ZrO_2, Fe_xO_y, Zr, Fe, SiO_2... in various proportions. In order to follow and record the corium flow, the test section is equipped with instrumentation composed of video cameras, pyrometers, infrared thermography, thermocouples, weighing scales.

2.2. Test description

Test VE-07 was carried out on the 4th and 5th November 1997. After two heating phases of around 45 min each at a maximum power of 190 kW, 25 kg of molten oxides were poured out of the furnace, 17.3 kg of which spread over a distance of 50 to 55 cm on a

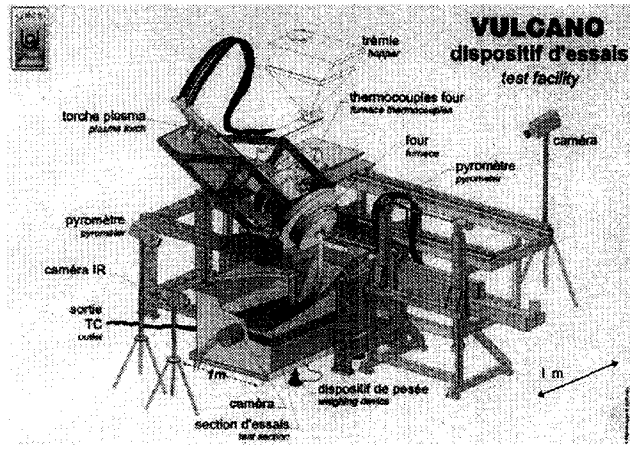

Figure 1. General view of the VULCANO facility.

spreading section made of zirconia bricks, on which a 19° sector had been delimited by magnesia bricks.

Folds are clearly visible on the surface of the spread melt (*figure 2*) which presents two lobes. The drag of a ∅ 1.5 mm immersed thermocouple — which did not work satisfactorily during the test — is also visible.

The initial melt composition has been determined to be the following, in mass: 33.3 % HfO_2 (hafnia), 22.2 % ZrO_2 (zirconia), 22.1 % SiO_2 (silica), 21.5 % $Fe_{0.947}O$ (wüstite) and 0.9 % CaO (lime).

This test is evidently on a much lower scale than what would hypothetically happen during a severe accident. Since Scale 1 experiments cannot be performed, the VULCANO facility is thus devoted to the validation of models and codes on a smaller scale.

2.2.1. On-line measurements

The mass flow rate varied around 2 $kg \cdot s^{-1}$ with a peak at 3.5 $kg \cdot s^{-1}$. This gives a volumetric flow rate of about 0.5 $L \cdot s^{-1}$. This is representative of the most conservative case for spreading, since a large flow rate would surely give an efficient spreading of the corium.

A pyrometer was used to monitor the melt temperature inside the furnace. It measured a surface temperature of 2 600 K while the plasma torches were operating and of 2 310 K when the furnace started to tilt. At this stage the plasma arc was no longer in operation.

An Ircon Mirage bichromatic pyrometer was aimed at the centre of the spreading section, at the level of its intersection with the inlet plane and a Maurer QPMR 465L bichromatic pyrometer was aimed horizontally (via a mirror) at the flow front (see *Figure 2*). *Figure 3* presents the read-outs from the pyrometers. The effect of the aluminium mirror reflectivities at both wavelengths has been corrected.

There is a good agreement between the measurements from the two sensors (less than 100 K difference), compatible with expected uncertainties and spatial heterogeneities; the differences between them are mainly

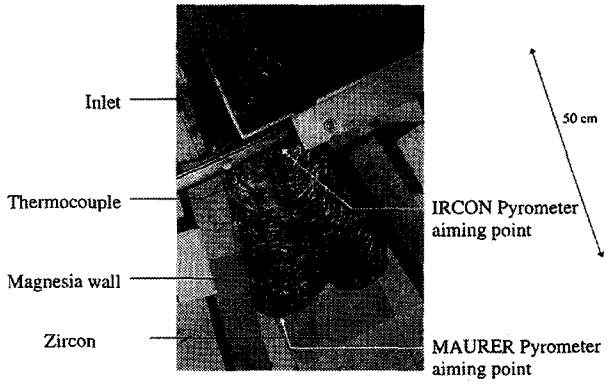

Figure 2. View of VE-03 spread.

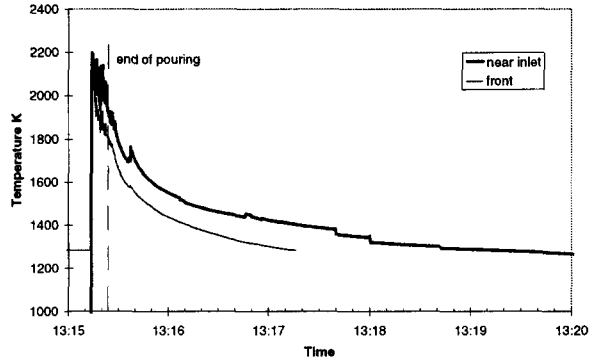

Figure 3. Measured front and inlet surface temperature.

due to the fact that the inlet was fed by hot corium while the front cooled rapidly. The maximum measured temperature is around 2 200 K.

Video and infrared cameras were also used to visualise the flow. It appears that the melt flowed onto the test section during roughly 8 s and then its front stopped its progression. This indicates that the front stopped before the end of the pouring sequence. The flow front velocity [4] remained below 15 $cm \cdot s^{-1}$, which corresponds to a Reynolds numbers of below 8 000, considering the spreading length (50 cm) as the characteristic length. This means that the flow can be considered laminar. When the flow progression stopped, the front surface temperature was around 1 800 K. It must be noted that the flow height at the front (20 mm) was three times larger than the capillary limit (7 mm). Dinh et al. [7] have proposed a scaling-law approach of spreading in which the main dimensionless parameter is the spread height relative to the capillary limit. It appears that this flow is more than 10 times thinner than what is typically expected during a hypothetical accident.

2.2.2. Physicochemical and thermodynamic analysis

The physico-chemical analysis and thermodynamic modelling of this test are reported elsewhere [8]. The main results are summarised in this section.

Figure 4, taken with a Scanning Electron Microscope, shows the difference of structure between the spread bulk, where the refractory oxide (Hf, Zr)O_2 has a globular shape and the surface where dendrites of this refractory oxide are observed.

At the top and bottom surfaces, 50 μm thick layers, in which iron has a different oxidation state, are observed : near the surfaces, iron is under the form of hematite (Fe_2O_3) — valence 3 — whereas in the rest of the spread, it is found in fayalite (2 FeO, SiO_2) in which it has a valence equal to 2. These oxidized layers can have a dramatic effect on the viscosity since in Urbain's model [9], which describes the viscosity of

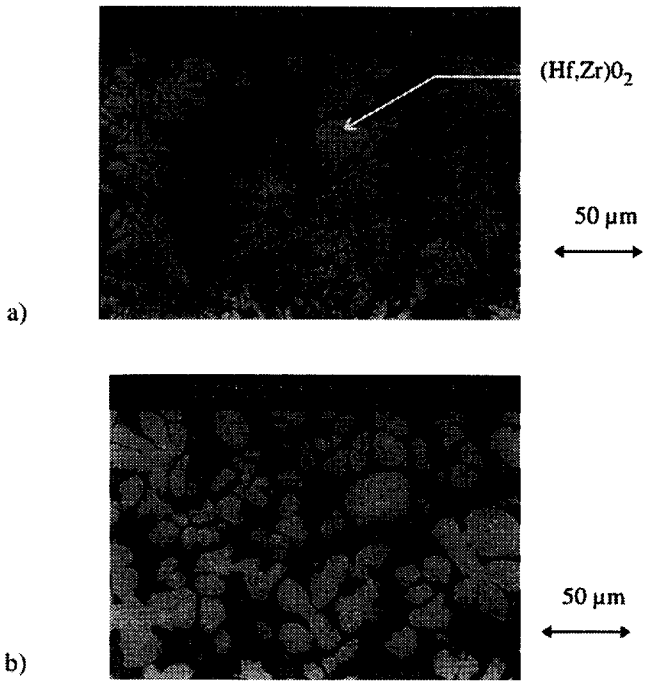

Figure 4. Microstructure as seen on SEM. **a.** Surface. **b.** Centre of the spread. Light coloured material: (Hf,Zr)O_2.

silicate mixtures, hematite is considered as amphoteric and, in our case, increases viscosity, whereas wüstite and fayalite are modifiers and decrease viscosity.

The thermodynamic modelling of the solidification process was performed using the Gibbs Enenergy Minimization code GEMINI 2 with the TDBCR981 database [10]. Because hafnium is not included in the database it was replaced by zirconium (mole by mole) since hafnia and zirconia form, in any proportion, a solidia solution [11].

Various computations have been made to take into account a 20 % oxygen atmosphere near the surface or the absence of atmosphere in the bulk, and equilibrium or rapid cooling configurations. We thus mainly present the results for the bulk of the spread melt (no oxygen and thermodynamic equilibrium) and indicate how the other cases differ from it.

The liquidus temperature was computed at around 2 370 K. Below 1 470 K the liquid fraction drops very significantly. However, the solidus temperature is only around 1 270 K.

Figure 5 shows the evolution of the solid volume fraction in the mixture assuming that there is no undercooling. Two types of calculations have been made: one assuming that, locally, the solidification occurred at thermodynamic equilibrium for each temperature (slow cooling), the other assuming a rapid cooling with no diffusion in the solid state (Scheill-Gulliver's model).

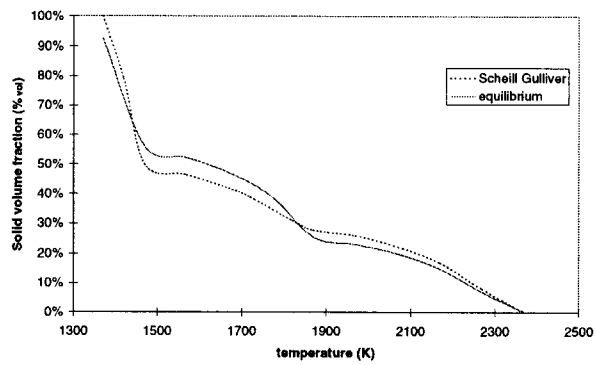

Figure 5. Local solid volume fraction versus temperature for 2 cooling models.

It appears that there is no significant change in the solid volume fraction between the two solidification patterns. The main difference is in the nature of the formed solid phase. This was experimentally confirmed in this test.

From these data it is possible to estimate the viscosity, using the methodology proposed by Sudreau et al. [12]. The viscosity in the bulk of the spread melt was estimated using Thomas' correlation [13] to take into account the effects of solid particles (at a volume fraction ϕ depending on temperature according to the thermodynamic model) on the relative viscosity μ_r.

$$\mu_r = 1 + 2.5\,\phi + 10.05\,\phi^2 + 0.00273\exp(16.6\,\phi) \quad (1)$$

This correlation has been validated over a wide range from 0 to 60 $\%_{vol}$ for suspensions of rigid inert spheres. Recent work on solidifying melts [14] suggests that Thomas's correlation underestimates the viscosity of this type of suspension. Nevertheless, it was applied to this study since it gives a conservative thickness of the rheological boundary layer. Moreover, we neglected the non-Newtonian effects [15] since very little is known about them for these types of fluids.

Following Shaw [16], we can approximate the viscosity in the melting range by an exponential law:

$$\mu = \mu^0\, e^{a(T_l - T)} \quad (2)$$

The rheological parameter a is an indicator of the sensitivity of the viscosity to temperature and is a complicated function of crystallinity and composition. Spera et al. [17] have verified that a relation of this type can describe the few silicate magma rheological data available in the literature. It is to be noted that for homogeneous melts at the super-liquidus temperatures, the temperature dependence is rather of the type:

$$\mu = A\, e^{B/T} \quad (3)$$

The viscosity, which has been computed assuming equilibrium thermodynamics, can be approximated by

an exponential law with a rheological parameter of 0.0081 K^{-1} with a correlation coefficient equal to 0.982:

$$\mu = 0.012\, e^{0.0081(T_{liquidus}-T)}\ (Pa{\cdot}s) \qquad (4)$$

This value is about 2.5 to 12 times lower than the 0.02 – 0.10 K^{-1} range that Spera et al. [17] compiled for basaltic magmas. This is due to the fact that the melting range is of more than 1 000 K in our case compared to 100–350 K ranges for natural magmas, and that natural magmas have a higher silica content than the VE-07 melt.

For the oxidised composition at the spread surface, the rheological parameter is higher (0.014 K^{-1}), due to the amphoteric properties of ferric oxide.

Below 1 450 K, the viscosity increases very sharply since most of the spread is solid.

3. THERMAL MODEL

The CRUST computer code has been developed to model the monodimensional transient behaviour of a corium-substratum multilayer system, taking into account the phase change but considering only thermal conduction in the melt and thermal radiation at the boundaries. An enthalpic formulation is explicitly solved:

$$H_i^{t+\delta t} = H_i^t + \frac{\lambda_i}{\rho}\frac{\delta t}{(\delta x)^2}(T_{i-1} - 2T_i + T_{i+1}) \qquad (2)$$

where H_i^t is the enthalpy of mesh i at time t, which is related to temperature T_i, λ_i is the thermal conductivity of the phase in mesh i, ρ is the specific mass (density changes at solidification are neglected except insofar as they affect the thermal properties), δt is the time increment, and δx is the mesh dimension.

For the mesh in which the phase-change front occurs, the method proposed by Tacke [18] is used. Temperature profiles are assumed to be linear in the liquid and solid regions near the front (*figure 6*). This enables the solid fraction to be computed in the mesh containing the front and thus the front position $X_{i0} + \xi\delta x$ with a sub-mesh resolution. The enthalpy of the mesh containing the solidification front, H_{i0}, is given by :

$$H_{i0}\,\delta x = L(1-\xi_s)\,\delta x + c_{pl}(T_{i0d} - T_f)(1-\xi_s)\,\delta x/2 - c_{ps}\,(T_f - T_{i0g})\,\xi_s\,\delta x/2 \qquad (3)$$

where L is the fusion latent heat, c_{ps} and c_{pl} respectively the solid and liquid phase specific heat, ξ_s the solid volume fraction in the mesh, T_f the fusion temperature, T_{i0d} and T_{i0g} the temperatures at the mesh boundaries which are obtained by linear interpolation. This yields a third degree equation which gives the solid volume fraction ξ_s in the mesh.

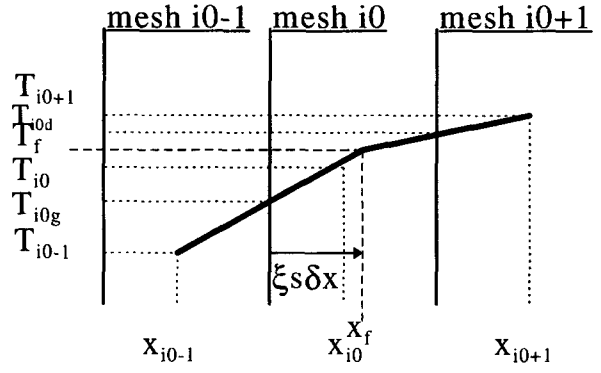

Figure 6. Temperature profiles used to determine the front position at sub-mesh resolution.

In our case, since we do not consider pure nor eutectic materials, the phase change does not occur at a given temperature but in a range of more than 1 000 K as shown in *figure 5*. The heat of fusion is in fact progressively released over this large temperature range as the liquid solidifies. The evolution of enthalpy versus temperature has been computed for the VE-07 mixture by GEMINI 2. In these computations, since the volumetric heat capacity ρc of hafnium and zirconium oxides is identical within 2.5 % — 2.475 $MJ{\cdot}m^{-3}{\cdot}K^{-1}$ at room temperature [20] — the density and specific heat of the mixture containing zirconium instead of hafnium have been used.

According to Jaeger [20], we define an *equivalent specific heat* which is the temperature derivative of the enthalpy. In other words, as stated by Kerr et al. [21], "the release of latent heat acts simply to increase the thermal inertia of the mushy layer". *Figure 7* presents the enthalpy and equivalent specific heat obtained from GEMINI2 computations.

The equivalent specific heat would exhibit a Dirac function during congruent solidification. In our case, it presents a maximum at three definite temperatures. The equivalent specific heat has been averaged over 1 530 K to 2 370 K: a value of 1 400 $J{\cdot}kg^{-1}{\cdot}K^{-1}$ has been taken for the sub-liquidus phase whereas the specific heat above liquidus is assumed constant at 850 $J{\cdot}kg^{-1}{\cdot}K^{-1}$. The behaviour below 1 530 K has not been modelled. The sub-liquidus equivalent specific heat can be understood as a combination of a 462 $kJ{\cdot}kg^{-1}$ latent heat, evenly distributed over the 1 530 K to 2 300 K solidification range, and of a constant 850 $J{\cdot}kg^{-1}{\cdot}K^{-1}$ specific heat.

The current version of the CRUST code allows for three superimposed layers, each of which can be partially liquid and partially solid (since we have extended a code developed for congruent solidification, the word solid is here improperly used to describe semi-solid material). At the upper interface, the system is cooled by radiation.

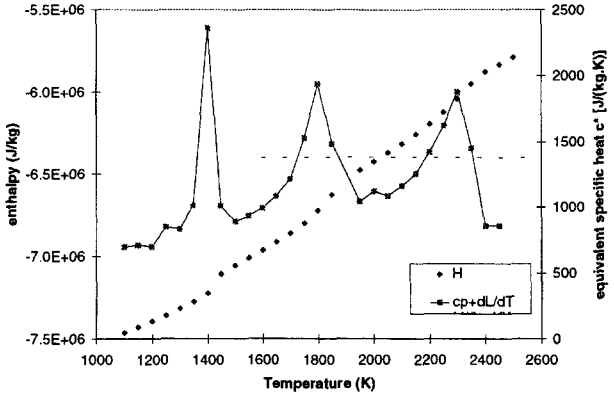

Figure 7. Enthalpy calculated by GEMINI 2 thermodynamics code (relative to the constituting elements at 273 K. The equivalent heat capacity ($c_p + \mathrm{d}L/\mathrm{d}t$) is the temperature derative of enthalpy. It has been averaged over the region of interest.

4. COMPUTATION OF SPREAD TEMPERATURE USING CRUST

4.1. Choice of physical properties

Two physical properties are poorly known for the thermal modelling of VE-07: surface emittance and thermal conductivity. It must be noted that the conduction model we use is only a simplification since there is some convection, both natural (due to the difference of density with temperature) and forced (due to the progression of the laminar flow and described in more detail by Griffiths and Fink [5] or by Dinh et al. [22]). The effect of porosity, including radiation in the pores at high temperatures (cf. Loeb [23]), should also be modelled. Nevertheless the conduction model gives an interesting insight into the behaviour if one uses, as Shaw et al. [24] in their modelling of lava lake cooling, an apparent conductivity chosen to include convection effects. Peck et al. [25] have experimentally shown the validity of such an approximate approach which requires fitting computation with measured data and can thus not be used for predictive calculations.

To assess the effect of thermal conductivity, various values of conductivity have been tested (*table I*). The computed surface temperatures are compared to the pyrometric measurement in *Figure 8* which has been zoomed over the 15 first seconds after the end of pouring. It is seen, as found by Peck et al. [25], that diminishing the conductivity gives a greater surface cooling. The values corresponding to cases 2 and 3 do not differ by a significant value, showing that the conductivity of the liquid phase does not significantly affect the surface. The rapid surface cooling and solidification implies that the greatest heat loss occurs through a solid crust, hence

TABLE I
Values of thermal conductivity used in the parametric analysis.

Case number	Liquid thermal conductivity ($\mathrm{W{\cdot}m^{-1}{\cdot}K^{-1}}$)	Solid thermal conductivity ($\mathrm{W{\cdot}m^{-1}{\cdot}K^{-1}}$)
1	3.0	3.0
2	1.5	1.5
3	3	1.5
4	1.5	3
5	2.5	2.5

the conductivity of the liquid is less important. Case 4 is also difficult to discriminate from cases 2 and 3.

To evaluate an apparent conductivity for the sub-liquidus range, temperature sensors at precisely known positions inside the melt would be necessary like those which Peck et al. [25] used in the Alae lava lake to obtain a very well fitted thermal model.

The preceding parametric analysis suggests that the "apparent" conductivity may be taken to be 2.5 $\mathrm{W{\cdot}m^{-1}{\cdot}K^{-1}}$ for both liquid and sub-liquidus phases, corresponding to "apparent" thermal diffusivities of 10^{-6} and $6{\cdot}10^{-7}$ $\mathrm{m^2{\cdot}s^{-1}}$.

The effect of emittance has been studied on case number 5. As the emittance increases, the heat flux extracted from the spread is greater and thus the cooling is faster. The slope at the initial instants is best fitted with an emittance of 0.8 ± 0.1.

For all the preceding computations, the initial temperature had been set at 2 423 K (average value of the furnace pyrometric readings). A test with a higher initial temperature (2 473 K) was performed. It appears that the initial temperature only has a very small effect on the surface temperature (after 10 s there is only a 14 K difference between the two simulations for an

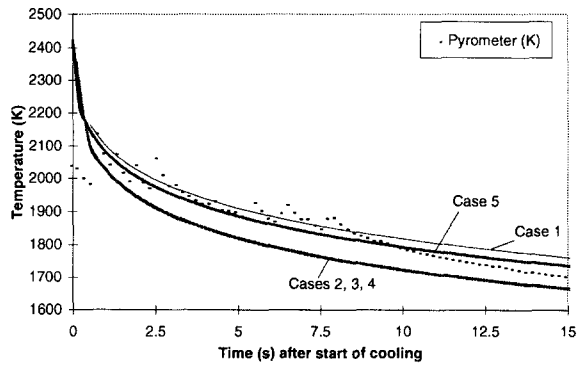

Figure 8. effect of thermal conductivity on CRUST computation of the surface temperature, compared to pyrometric measurements at the section entrance.

initial difference of 50 K). It will thus be quite difficult to obtain a good estimate of the initial temperature from the fitting of surface cooling curves. An initial temperature of 2 423 K (corresponding to 50 K above liquidus is arbitrarily taken for the remainder of this analysis.

The agreement between the model and the measurement cannot be perfect because the initial melt temperature was not constant due to the rupture of the plasma arc before pouring and also because the cooling was not uniform as shown by the 50 K increase appearing in *figure 2* at $t = 18$ s. This is attributed to the arrival of a small "splash" of corium at the pyrometer aiming point.

Other physical phenomena such as undercooling and convection are not modelled by this simple code. Moreover, the method to determine the physical properties is far from being rigorous. Inverse methods should be used and more measurement points would be apreciated. Genetic algorithms [26] could be an option to reliably estimate corium thermal properties with CRUST computations.

Nevertheless, the method described here gives a set of properties which is coherent with measurements and which can thus be used to estimate the thermal evolution of the flow in points where there were no sensors.

TABLE II
Numerical data corresponding to case 5

Meshes	
height of top layer (m)	$1.000 \cdot 10^{-2}$
mesh step for top layer (m)	$1.000 \cdot 10^{-4}$
Physical data	
T_f liquidus temperature K	$2.370 \cdot 10^{3}$
Liquid	
Thermal conductivity ($W \cdot m^{-1} \cdot K^{-1}$)	2.500
specific mass ($kg \cdot m^{-3}$) [taking porosity into account]	$3.000 \cdot 10^{3}$
Equivalent specific heat ($J \cdot kg^{-1} \cdot K^{-1}$)	$8.500 \cdot 10^{2}$
Semi-solid	
Thermal conductivity ($W \cdot m^{-1} \cdot K^{-1}$)	2.500
Specific mass ($kg \cdot m^{-3}$)	$3.000 \cdot 10^{3}$
Specific heat ($J \cdot kg^{-1} \cdot K^{-1}$)	$1.400 \cdot 10^{3}$
Load	
Initial temperature (K)	$2.423 \cdot 10^{3}$
Boundary temperature at the lower interface (K)	$2.423 \cdot 10^{3}$
Radiation	
Emissivity of top surface	$0.800 \cdot 10^{0}$

Table II presents the data used for the configuration which was found to give the smallest discrepancy between measurement and computation. The corium and the substratum were assumed, in most of this study, to initially be at the same temperature, in order to only analyse the effect of radiation cooling at the upper surface of a corium spread. The time step and the mesh dimensions have been verified to be small enough to prevent discretization effects.

4.2. Temperature profile in the oxidic spread

In this section we will compute the temperature profile, using CRUST, with the values of emittance, conductivity and initial temperature estimated from the last section. In order to assess the effects of an error on this estimation, a sensitivity analysis is first presented.

4.2.1. Sensitivity analysis

Figure 9a shows that if a conductivity of 1.5 $W \cdot m^{-1} \cdot K^{-1}$ is assumed instead of 3.0 $W \cdot m^{-1} \cdot K^{-1}$, there will be a deviation of 100 K on the temperature 1 cm below the surface, 1 min after the beginning of cooling. This deviation is of the same magnitude as that observed on the surface temperature, but in the opposite direction: the smaller conductivity leading to the hotter temperatures as reported by Peck et al. [25].

The effect of emittance is less sensitive: a 20 % deviation of the emittance results in a very small difference (less than 20 K) at 1 cm below the surface. An error in the estimation of the initial temperature leads, for the temperatures computed both at the surface and 10 mm below, to a deviation diminishing with time (see *figure 9b*).

In the following paragraphs, we will use the data set from case number 5 (conductivity of 2.5 $W \cdot m^{-1} \cdot K^{-1}$ for both phases, emittance 0.8, initial temperature 2 423 K). If the exact values are in the range studied in § 0, the qualitative results from the analysis detailed in the following sections will remain valid.

4.2.2. Temperature computations

Figure 10 presents the progression with time of the liquidus isotherm. The liquidus front progresses towards the centre of the spread at a speed of roughly 0.3 $mm \cdot s^{-1}$, except in the first seconds when it goes faster. It reaches 10 mm in 25 s. This curve is best fitted with a power law with an exponent of 0.59, whereas the analytical model with no phase change and constant specific heat gives a solution which varies at the first order as a square root (Carslaw and Jaeger [27], pp. 70–71). In the case of convection, Kerr et al. [21] have shown that the liquidus isotherm does not

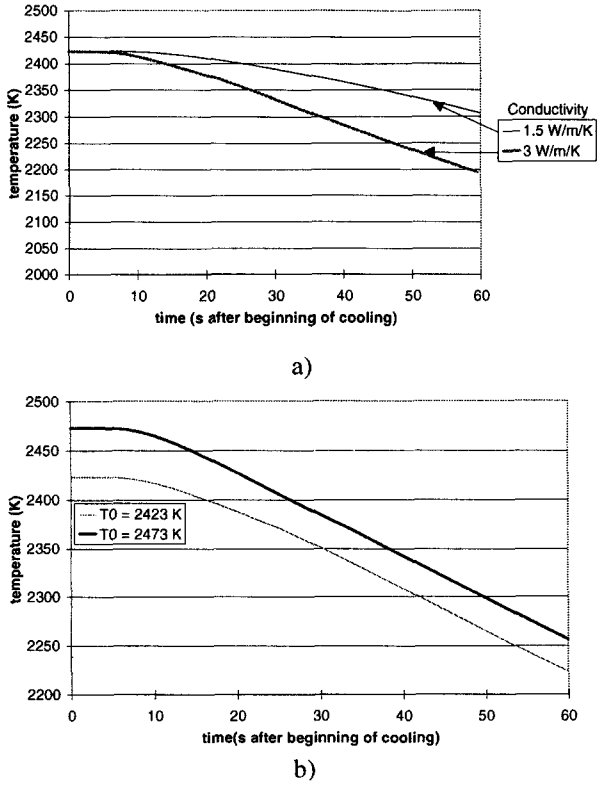

Figure 9. Effect of uncertainty on the temperature estimated 10 mm below the surface. **a.** Effect of thermal conductivity. **b.** Effect of initial temperature.

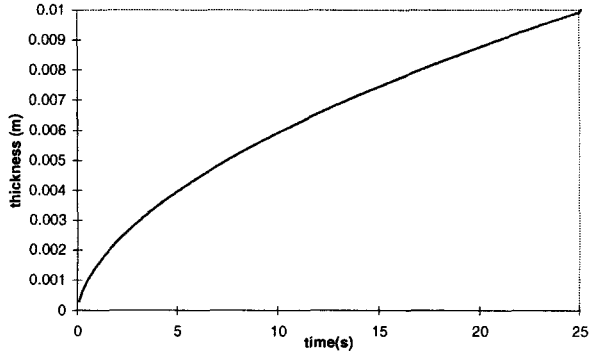

Figure 10. Estimation of the liquidus-isotherm progression inside the melt.

generally follow a square root law. However, they have shown, for the beginning of the cooling phase, that the main heat balance is between the conduction through the mushy layer and the removal of latent and specific heat from the growing solid. This is valid in the first 10 s, when there is a flow, and gives an interface depth that is close to what is computed by a conduction model.

Figure 11 presents the temperature computed for each of the ten millimetres below the surface. Dendrites were observed only in the uppermost millimetre. In the lower regions, where the cooling rate has always been below 100 $K \cdot s^{-1}$, even in the first second, only globules were observed. In comparison, there is a cooling of 350 K during the first second at the surface where dendrites are observed.

In the upper 3 mm of the spread, there is a very quick cooling in the first 5 to 10 s (40 $K \cdot s^{-1}$ at 1 mm and 30 $K \cdot s^{-1}$ at 2 mm) and then a slower cooling (5 $K \cdot s^{-1}$). For the deeper layers of the melt, there is a propagation delay before the cooling front reaches the inner layers. When it does, the cooling is slower (around 5 $K \cdot s^{-1}$). It must be noted that the curves have an upward concavity to a depth of 5 mm and a downward concavity for the deeper regions.

From *figure 11*, the temperature profiles at 4 characteristic instants (1, 5, 10 and 20 s after the beginning of cooling) have been extracted and plotted in *figure 12*. This *figure* shows the growth of a thermal boundary layer below the spread surface. Its thickness, which could for instance be defined as the thickness at which

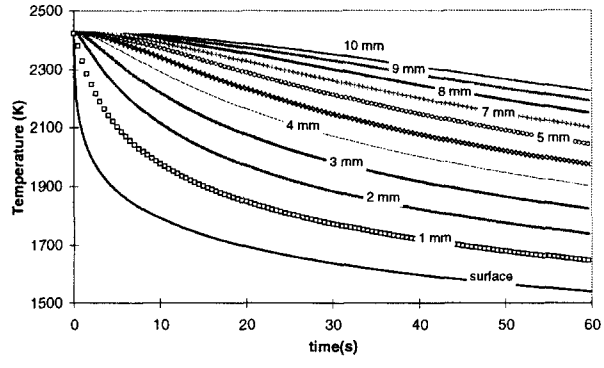

Figure 11. Estimation of the temperature at each of the first 10 mm under the melt surface.

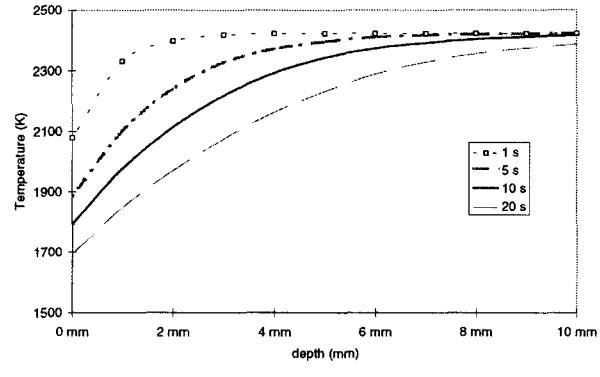

Figure 12. Temperature profiles at 1 s, 5 s, 10 s and 20 s after the beginning of cooling.

the temperature deviates by more than 2.5 % from the bulk temperature, equals 1 mm after 1 s of cooling and reaches 5 to 6 mm after 10 s. It will reach the centre of the spread after about 30–50 s, i.e. after the end of the flow in our experiments.

4.3. Physico-chemical boundary layer

The compositions at thermodynamic equilibrium computed for each temperature can now be used to convert the temperature data into solid fraction, composition and physical properties during the cooling phase. This means that solidification occurred more or less at equilibrium and that the undercooling was low. This is rather questionable because relatively high cooling rates are observed near the surface and this generally implies high undercooling [28]. Moreover, dendrites have been observed in the uppermost millimetre and solid solutions of hafnon and zircon (which are predicted by the equilibrium hypothesis) have not been found in most of the samples. Nevertheless, since we have seen in § 2.2.2 that there is little difference, in terms of solid volume fraction, between the equilibrium and the Scheill-Gulliver hypothesis, we will use the equilibrium data in this section. Undercooling would shift the results presented in this section towards the low temperatures.

The solid volume fraction has been plotted versus time at various depths in *figure 13a*. The change of slope at 20 $\%_{vol}$ is due to the plateau between 1 870 and 2 070 K, where the solid volume fraction remains relatively constant. This could actually be a computation artefact due to the fact that the equivalent specific heat has been modelled as a constant throughout the solidification range. In fact, equivalent specific heat presents a local minimum around 2 000 K at about 1 000 $J{\cdot}kg^{-1}{\cdot}K^{-1}$ — compared to the average value of 1 400 $J{\cdot}kg^{-1}{\cdot}K^{-1}$ —, which is due to the fact that the contribution of latent heat is minimum in this range since only a minute fraction of the fluid is solidified between 1 870 and 2 070 K.

Spohn et al. [29] nevertheless observed this type of plateau when they computed the crystallization of a bi-component mixture, including the effects of undercooling. They concluded that one of the differences between a one-component substance and two or more component melts of substances that do not form one solid solution, is that the former crystallizes in one step while the latter takes at least two steps to crystallize.

Figure 13b presents, at given instants, an idea of the solidification versus depths in the spread. In the melt upper millimetres, the initial solidification speed (30 $\%_{vol}/s$ at the surface) while it is slower in the bulk (0.5 $\%_{vol}{\cdot}s^{-1}$ at 10 mm). The transition between dendritic and globular crystals is found at around a depth of 1 mm. It corresponds to a crystallization speed of above 5 $\%_{vol}{\cdot}s^{-1}$.

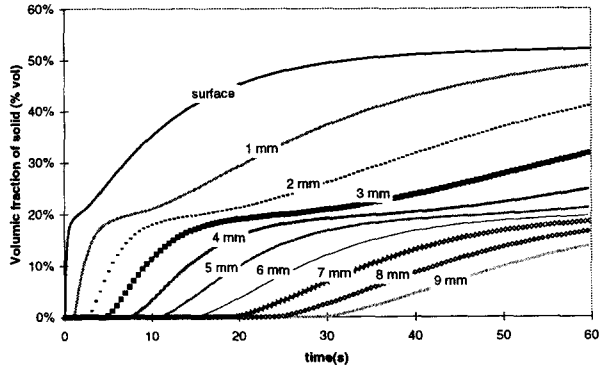

a)

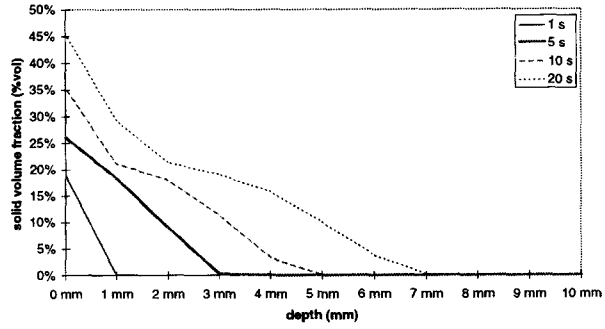

Figure 13. Computed solid volume fractions. **a.** Computation at the upper millimetres. **b.** Values at 4 characteristic instants.

The spreading flow stopped after less than 10 s. At this time, the calculated temperature (1 800 K) leads to an estimated solid volume fraction at the surface of 35 $\%_{vol}$ and to a solid mass fraction of around 50 $\%_{w}$. The front temperature at the end of the flow progression was also measured at 1 800 K.

The gradual change of phase which occurs during solidification, coupled with the thermal contraction of the mixture constituents, generates important variations in the mixture density with temperature. The effects of density change during the fractional crystallization have been thoroughly studied by Sparks and Huppert [30] in the case of basaltic magmas.

If the assumption is made that the partial molar volume of any component is independent from bulk composition (Nelson and Carmichael [31]), the GEMINI 2 code output can be used to estimate the density of the liquid and solid phase for any temperature. *Figure 14* presents the results assuming the rapid cooling

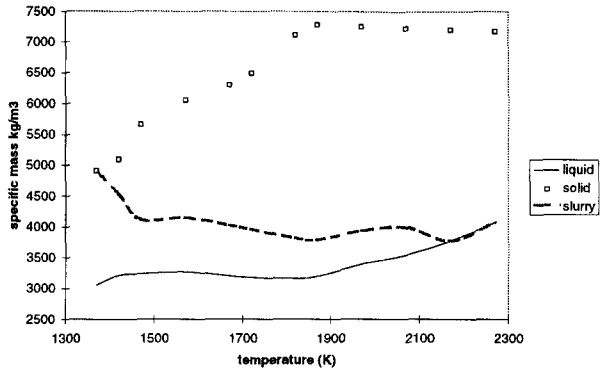

a)

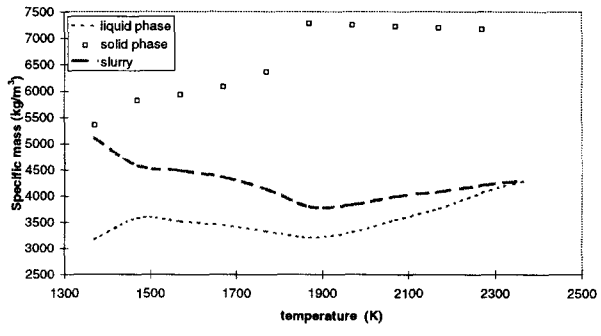

b)

Figure 14. Density evolution for the liquid and solid phases, and for the slurry made by the mixture of both. a. Rapid cooling (Scheil Gulliver). b. Local thermodynamic equilibrium.

hypothesis (Scheil Gulliver model with GEMINI 2 code) or thermodynamic equilibrium.

At high temperatures, the solid phase is made only of a (heavy) solid solution of zirconia and hafnia. Below 1 870 K, a (lighter) solid solution of hafnon and zircon is formed. In the Scheill Gulliver model, since solid phase diffusion is assumed to be absent, only the part that remains liquid at 1 870 K is available to form these silicates. This explains the difference of shape in the density curves.

These density data were then applied to the temperature computations shown in the preceding section. The Scheil Gulliver model is the more relevant to describe the rapidly cooled boundary layer. The density of the fluid exhibits small scale oscillations which are not favourable to the onset of natural convection over the whole melt height.

4.4. Rheological boundary layer

The compositions and solid fractions computed in the preceding section can also be related to the oxidic spread rheological properties. Viscosity varies over more than 6 decades in the solidification range.

Figure 15 presents the viscosity computed on the 10 upper millimetres of the melt from CRUST temperature outputs using the simplified exponential law. The surface viscosity has been computed for both ferric and ferrous compositions. The presence of a rheological boundary layer is clearly shown in this *figure*.

Figure 16 shows the viscosity profiles 1, 5, 10 and 20 s after the beginning of cooling, in logarithmic scales. The uppermost millimetre forms a rheological boundary layer in the melt which propagates downwards as it cools. If we compare these curves with the temperature curves from section 0, it appears that, at the same time, the thermal boundary layer is roughly three times larger than the rheological boundary layer. This is coherent with the observation of Tozer [32] which asserted that

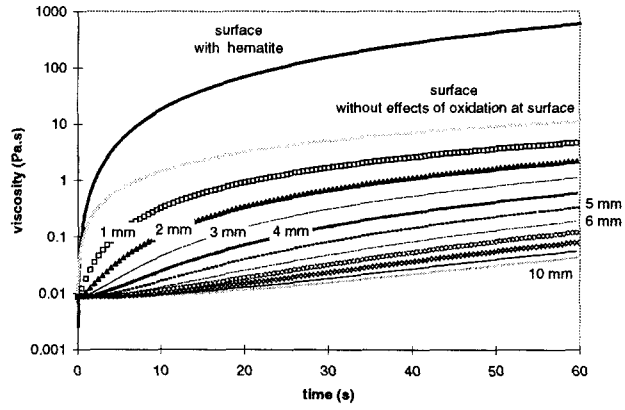

Figure 15. Viscosity estimates (Thomas' correlation). For the surface layer, the estimation has been made for the two possible oxidation states.

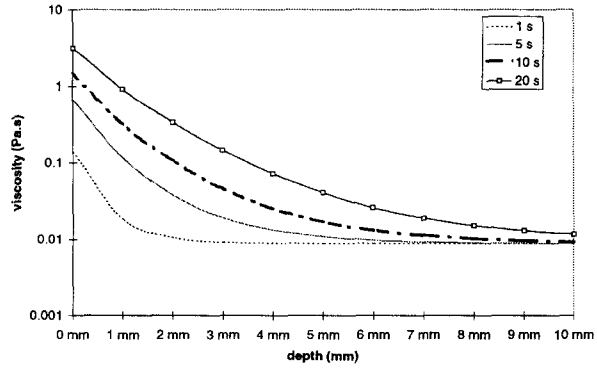

Figure 16. Viscosity profiles at various instants.

Figure 17. Ropy pahoehoe flow on Kilauea volcano, 1987. The corrugated features are comparable to those observed in figure 1. Photography by D.J. Johnson.

this ratio is equal to the square root of the Prandtl number of the medium $\mu/(\kappa\rho)$ – in our case Pr#10.

If a ferric composition is taken into account for the upper 50 μm, it appears that even 2 s after the beginning of cooling the effect of oxidation is significant. But the latter affects less than 50 μm at the upper surface. Even without taking into account the effects of oxidation, there is a very sharp viscosity contrast between the interior of the flow and its free surface. This effect must be taken into account in the spread modelling, especially when 1-D or horizontal 2-D meshes are used.

5. SURFACE FOLDING AND DEPTH-DEPENDENT RHEOLOGY

The surface of the VE-07 spread appears to be significantly corrugated. The surface is regularly folded and presents folds with an upstream concavity. The same type of surface is found on the so-called *ropy pahoehoe* lavas (*figure 17*) which are associated with low velocity volcanic lava flows. In this case, the crust is not disrupted and is crumbled within channels in close series of pleats.

Griffiths and Fink [33] have determined that the major changes in the morphology of lava flows occurred at fixed values of the dimensionless number Ψ defined as the ratio of the time taken for a solid crust to form on an element of lava (50 s are needed in VE-07 to reach 1 500 K) to the characteristic time for horizontal advection of lava (practically 5 s for VE-07). They stated that the ropy structure appeared for the $10 < \Psi < 25$ range. For VE-07, we had $\Psi = 10$.

The main feature of the ropy structure is the rather regular spacing of the folds. VE-07 pleats have a wavelength of between 7 and 10 mm and a depth of between 1.5 and 3.5 mm. For basaltic pahoehoes, the scale length is larger (wavelengths can be between 0.1 and 3 m for heights of a few centimetres [34]; 50 m long ridges can even be interpreted as folds [35]). The characteristic dimension of this phenomenon is the fold arc length, which in the VE-07 case ranges between $\mathcal{L} = 10$ mm to $\mathcal{L} = 15$ mm.

As the ropes form, the partly cooled corrugated sections move downstream from their formation site, the individual cords are elongated and are rotated away from the midline of the channel so that the corrugation train acquires a parabolic aspect with the upstream concavity.

Biot [36] has theoretically derived the following relationship for the dominant wavelength $\mathcal{L}$ in the case of a thin layer of viscosity μ and of thickness H over a medium of viscosity μ', assuming slip at the layer-medium interface and no uniform compression in the medium.

$$\mathcal{L} = 2\pi H \sqrt[3]{\mu/6\mu'} \tag{6}$$

Let us consider that the bulk of the spread has a constant viscosity of 0.01 Pa·s and that the rheological layer has a viscosity of 0.3 and 1 Pa·s (corresponding to the value computed for the ferrous surface 2 and 10 s after the beginning of cooling; for the ferric composition, the viscosity is between 1 and 12 Pa·s). The layer height being around 1 mm, the calculated wavelength is between 10 and 16 mm, which corresponds well to the measured arc lengths. If the oxidised surface viscosity is used in formula (6), larger $\mathcal{L}/H$ ratios (16 to 40) are found, but it is clear that a smaller equivalent height must be considered since only a portion of the viscous boundary layer is found at these high viscosities.

Fletcher [37] analysed the case of the folding of a single viscous layer and found exact infinitesimal amplitude solutions. For $\mu > 10\mu'$, the difference between Biot's formula and the exact formulation for both slip and no-slip interfacial conditions is negligible. Thus Biot's formula can be used in our case.

Actually, there is not a uniform-viscosity upper layer but rather a continuous decrease of viscosity from the surface to the spread interior. An appropriate model will therefore consist of a layer in which the viscosity decreases rapidly with depth, lying above a fluid with a uniform viscosity which can be treated as infinitely deep. The only continuous variation in viscosity for which the mechanical analysis is tractable is one in which the viscosity decreases exponentially with depth (Fink and Fletcher [34]).

The viscosity is thus assumed to be described by the following equations:

$$\mu(z) = \begin{cases} \mu^0 e^{\gamma z} & -H \leqslant z \leqslant 0 \\ \mu_i \ (= \mu^0 e^{-\gamma H}) & z < -H \end{cases} \tag{7}$$

Table III summarises the properties of the rheological boundary layer at various instants. It can be noted that

TABLE III
Properties of the rheological boundary layer at successive instants: interior, surface viscosity, rheological boundary layer height and exponential decay and dimensionless wavelength.

Time (s)	μ^0 (Pa·s)	μ_i (Pa·s)	H (mm)	γ (m^{-1})	$\mathcal{L}\gamma$
1	0.14	0.09	$\approx$ 1.3	340	3.5–5
2	0.27	0.09	1.7	650	6.5–10
5	0.68	0.09	2.3	900	9–13.5
10	1.45	0.09	3.5	800	8–12
20	3.18	0.09	5.0	700	7–10.5

the value of γ has been estimated between 130 and 2 300 m^{-1} for Kilauea lavas.

Fink and Fletcher [34] have shown that folding can occur without the presence of a discontinuity between the flow interior and a plastic "crust". They proposed, as a criterion for folding not to decay, that an amplification factor q be greater than 10. This requires that the dimensionless wavelength $\mathcal{L}\gamma$ (product of the arc length by the viscosity exponential decay parameter) be greater than 15. In other words, when an instability appears at the spread surface, as when there is a change of slope, if the dimensionless wavelength is large enough it will remain and be convected. In the case of VE-07, surface instabilities are thought to have been caused by the change of slope at the spreading plane inlet and by the presence of intrusive instrumentation.

It appears that the dimensionless wavelength is slightly below the limit proposed by Fink and Fletcher. Since the amplification factor limit of 10, leading to a dimensionless wavelength of 15, was arbitrary, these values are still consistent with a folding caused by a viscous boundary layer. Moreover, the fact that the viscosity correlation used has only been validated on rigid spheres and is believed to underestimate reality in the case of solidifying crystals [14] must be taken into account. Also, the effect of a thin viscous layer due to the oxidation of iron oxides can be assimilated to a steeper gradient and could give a larger dimensionless wavelength, which would be more within the limits given by Fink and Fletcher. Finally, the presence of dendrites in the upper millimetre should also increase the viscosity of the suspension as it was shown by Flemmings [37].

The data from test VE-07 are thus, within these uncertainties, coherent with the theory proposed by Fink and Fletcher [34].

6. CONCLUSION

Experimental data from the VE-07 VULCANO test have been used to fit the physical parameters of a conduction heat transfer model using the CRUST computer code. Satisfactory fit was obtained for an emittance of 0.8 and an apparent thermal conductivity of 2.5 $W{\cdot}m^{-1}{\cdot}K^{-1}$. This latter value takes into account the convection in the liquid part of the spread and the radiation inside the porosities.

With this data set it was possible to estimate the properties of the spread melt at various depths as it cools down. The liquidus isotherm progresses towards the centre of the spread with an initial speed of 0.3 mm/s. The thermal boundary layer reaches roughly 5 mm after 10 s of cooling. The cooling rates are quite high (40 to 100 $K{\cdot}s^{-1}$ at 1 mm depth) near the surface, whereas they are slower inside the melt ($\approx$ 5 $K{\cdot}s^{-1}$), the latter starting to cool only after the time needed for the heat front to propagate.

These temperature data can then be used to estimate the physical properties of the solidifying fluid, assuming equilibrium cooling or using the Scheill-Gulliver model. Solidification fronts travelling at rates greater than 5 $\%_{vol}$ per second have been estimated. Density gradients inside the melt due to temperature gradients have also been evaluated.

There are very steep viscosity gradients in a boundary layer, which can be approximated by an exponential law with an exponential decay of about 800 m^{-1}. As stated by Spera et al. [17], extreme caution must therefore be exercised in using a constant viscosity boundary layer theory to model phenomena when a large viscosity contrast exists across the thermal boundary layer.

One of the clearly visible effects of this viscous boundary layer is the folds on the surface of this spread. These can be compared to the folds found on "ropy pahoehoe" lavas. The order of magnitude of the dimensionless wavelength of these folds is consistent with the model proposed by Fink and Fletcher [34].

Due to the measurement limitations, it is unavoidable that such an analysis contain large uncertainties and the results must be understood as orders of magnitudes and phenomenological descriptions rather than precise values.

This work must be pursued by a complete analysis taking into account the effects of the interface between substratum and spread. The amount of undercooling and its effects must also be estimated from the VULCANO spreading experiments in order to test the results of this type of computation. The effects of porosity and gases in the melt must also be investigated to obtain a better physical understanding of the physical phenomena occuring during corium spreading. This knowledge will then be coupled with a hydrodynamic analysis in order to improve the spreading modelling.

Acknowledgements

This work was partially funded by the European Commission under contract FI4S-CT96-0041 (Corium Spreading & Coolability Project).

The authors greatly acknowledge the work and efforts of the whole VULCANO team.

REFERENCES

[1] Weißhäupl H.A., Severe accident mitigation concept of EPR, Nuclear Eng. Design, 187 (1999) 35–45.

[2] Cognet G., Seiler J.-M., Szabo I., Latché J.-C., Spindler B., Humbert J.-M., La récupération du corium hors cuve, Revue Générale Nucléaire (1) (1997) 38–43.

[3] Gatt J.-M., Buffe L., Marchand O., Numerical modelling of the corium-substratum system, in: Proc. 13th Int Conf Structural Mech. Reactor Technol. (SMIRT 13), Porto Allegre, Brazil, 1995.

[4] Journeau C., Jung Y., Pierre J., Visualization of a 2 000 °C melt spreading over a plane, in: Proc. 8th Int. Symp. Flow Visualization, Sorrento, Italy, 1998.

[5] Griffiths R.W., Fink J.H., Effects of surface cooling on the spreading of lava flows and domes, J. Fluid Mech. 252 (1993) 667–702.

[6] Jégou C., Cognet C., Roubaud A., Gatt J.-M., Laffont G., Kassabji F., Plasma transferred arc rotary furnace for corium melting, J. High Temp. Mater. Proc. 3 (1998)

[7] Dinh T.N., Konovalikhin M., Paladino D., Green J.A., Gubaidulin A., Sehgal B.R., Experimental simulation of core melt spreading on a LWR containment floor in a severe accident, in: Proc. 6th Int. Conf. Nuclear Eng., ICONE-6, San Diego, CA, 1998

[8] Sudreau F., Journeau C., Cognet G., Physico-chemical analyses and study of the solidification of multi-component melt spreads, Mater. Sci. Eng. (submitted).

[9] Urbain G., Bottinga Y., Richet P., Viscosity of liquid silica, silicates and alumino-silicates, Geochim. Cosmochim. Acta 46 (1982) 1061–1072.

[10] Thermodata, Thermochemical equilibria calculation code: complex multi-component phases: GEMINI 2, Thermodata, BP 66, 38402 Saint-Martin-d'Hères cedex, France, 1997.

[11] Ruh R., Garett H.J., Domagala R.F., Talan N.M., The system zirconia-hafnia, J. Am. Ceram. Soc. 51 (1968) 23–27.

[12] Sudreau F., Ramacciotti M., Cognet G., Seiler J.-M., Calculation Methodology for corium viscosity, Mater. Sci. Eng. (submitted)

[13] Thomas D.G., Transport characteristics of suspensions: a note on the viscosity of Newtonian suspensions of uniform spherical particules, J. Colloid. Sci. 20 (1965) 267–277.

[14] Ramacciotti M., Journeau C., Abbas G., Werozub F., Cognet G., Propriétés rhéologiques de mélanges en cours de solidification, Cahiers de Rhéologie XVI (1998) 303–316.

[15] Griffiths R.W., Fink J.R., Solidifying Bingham extrusions: a model for the growth of silicic lava domes, J. Fluid Mech. 347 (1998) 13–36.

[16] Shaw H.R., Rheology of basalt in the melting range, J. Petrol. 10 (3) (1969) 510–535.

[17] Spera F.J., Yuen D.A., Kirschvink S.J., Thermal boundary layer convection in silicic magma chambers: effects of temperature dependant rheology and implications for thermogravitational chemical fractionation, J. Geophys. Res. B 87 (1982) 8755–8767.

[18] Tacke K.-H., Discretization of the explicit enthalpy method for planar phase change, Int. J. Numer. Meth. Eng. 21(1985) 543–554.

[19] K&K associates; Materials Properties II, ver. 1.02, http ://www.kassoc.com/, 1997.

[20] Jaeger J.C., Cooling and Solidification of Igneous Rocks, in: Hess H.H. and Poldervaart A. (Eds.), Basalts: the Poldervaart Treatise on Rocks of Basaltic Composition, vol. 2, John Wiley Interscience, New York, 1967, pp. 503–536.

[21] Kerr R.C., Woods A.W., Worster M.G., Huppert H.E., Disequilibrium and macrosegregation during solidification of a binary melt, Nature 340 (1989) 357–362.

[22] Dinh T.N., Dong W.G., Green G.A., Nourgaliev R.R., Sehgal B.R., Melt jet attack of the reactor vessel wall: phenomena and prediction method, in: Proc. 8th Int. Topical Mtg. Nuclear Reactor Thermal Hydraulics, NURETH-8, Kyoto, Japan, 1997, pp. 612–619.

[23] Loeb A.L., Thermal Conductivity. VIII. A Theory of Thermal Conductivity of Porous Materials, J. Am. Ceram. Soc. 37 (1954) 96–99.

[24] Shaw H.R., Hamilton M.S., Peck D.L., Numerical analysis of lava lake cooling models. Part I. Description of the method, Am. J. Sci. 277 (1977) 384–414.

[25] Peck D.L., Hamilton M.S., Shaw H.R., Numerical analysis of lava lake cooling models. Part II. Application to Alae lava lake, Hawaii, Am. J. Sci. 277 (1977) 415–437.

[26] Garcia S., Guynn J., Scott E.P., Use of genetic algorithms in thermal property estimation. Part II. Simultaneous estimation of thermal properties, Numer. Heat Tr. A 33 (1998) 149–168.

[27] Carslaw H.S., Jaeger J.C., Conduction in solids, Clarendon Press, Oxford, 2nd Ed., 1959.

[28] Kurz W., Fisher D.J., Fundamentals of Solidification, Trans Tech Publications, Ädermannsdorf, CH, 1992.

[29] Spohn T., Hort M., Fischer H., Numerical simulation of the crystallization of multicomponent melts in thin dikes or sills. 1. The Liquidus phase, J. Geophys. Res. B 93 (1988) 4880–4894.

[30] Sparks R.S.J., Huppert H.E., Density changes during the fractional crystallization of basaltic magmas: fluid dynamic implications, Contrib. Mineral. Petr. 85 (1984) 300–309.

[31] Nelson S.A., Carmichael I.S.E, Partial molar volume of oxide components in silicate liquids, Contrib. Mineral. Petr. 71 (1979) 117–124.

[32] Tozer D.C., Thermal plumes in the Earth's mantle, Nature 244 (1973) 394–400.

[33] Griffiths R.W., Fink J.H., The morphology of lava flows in planetary environments: predictions from analog experiments, J. Geophys. Res. B 97 (1992) 19739–19748.

[34] Fink J.H., Fletcher R.C., Ropy pahoehoe: surface folding of a viscous fluid, J. Volcanol. Geotherm. Res. 4 (1978) 151–170.

[35] Fink J., Surface folding and viscosity of rhyolite flows, Geology 8 (1980) 250–254

[36] Biot M.A., Folding instability of a layered viscoelastic medium under compression, Proc. R. Soc. London, Ser. A, 242 (1957) 444–454.

[37] Fletcher R.C., Folding of a single viscous layer: exact infinitesimal-amplitude solution, Tectonophysics 39 (1977) 593–606.